Hyperspectral three-dimensional absorption imaging using snapshot optical tomography

Cory Juntunen,¹ Andrew R. Abramczyk,¹ Isabel M. Woller,² and Yongjin Sung^{1, *}

¹College of Engineering and Applied Science, University of Wisconsin, Milwaukee, Wisconsin 53211, USA

²College of Health Sciences, University of Wisconsin, Milwaukee, Wisconsin 53211, USA

(Dated: August 29, 2022)

Hyperspectral imaging (HSI) records a series of two-dimensional (2D) images for different wavelengths to provide the chemical fingerprint at each pixel. Combining HSI with a tomographic data acquisition method, we can obtain the chemical fingerprint of a sample at each point in three-dimensional (3D) space. The so-called 3D HSI typically suffers from low imaging throughput due to the requirement of scanning the wavelength and rotating the beam or sample. In this paper we present an optical system which captures the entire four-dimensional (4D), i.e., 3D structure and 1D spectrum, dataset of a sample with the same throughput of conventional HSI systems. Our system works by combining snapshot projection optical tomography (SPOT) which collects multiple projection images with a single snapshot, and Fourier-transform spectroscopy (FTS) which results in superior spectral resolution by collecting and processing a series of interferogram images. Using this hyperspectral SPOT system we imaged the volumetric absorbance of dyed polystyrene microbeads, oxygenated red blood cells (RBCs), and deoxygenated RBCs. The 4D optical system demonstrated in this paper provides a tool for high-throughput chemical imaging of complex microscopic specimens.

I. INTRODUCTION

Absorption spectroscopy is one of the most widely used techniques for analytical chemistry[1]. For a homogeneous sample with known thickness (e.g., solution in a cuvette), the ratio of incident to transmitted light intensity is measured for varying wavelengths. The absorption spectrum can provide the types and concentrations of various atoms and molecules in the sample. For a sample that is homogeneous along the light propagation direction but heterogeneous in the transverse directions, hyperspectral imaging can provide the absorption spectrum at each pixel in the two-dimensional (2D) image. This, however, requires the thickness at each pixel is given or measured with complementary methods such as atomic force microscopy[2]. Various efforts have been made to increase the speed of hyperspectral imaging at the cost of spectral resolution[3, 4]. Snapshot hyperspectral imaging has also been demonstrated using various methods such as a computer-generated hologram[5] or a coded aperture[6]. For a sample heterogeneous along all three dimensions, hyperspectral three-dimensional (3D) imaging is necessary. To obtain the absorption spectrum at each voxel within the sample's volume, 3D imaging can be performed for varying wavelengths of the incident light, which provides a four-dimensional (4D) data cube. For the 3D imaging, a series of 2D images, called projection images, is typically recorded while rotating the sample (sample-rotation tomography) or varying the angle of the incident beam onto the sample (beam-rotation tomography)[7]. The 3D absorption map at the selected wavelength can be calculated by applying a tomographic

reconstruction algorithm to the projection images. This tomographic measurement of 3D absorption coefficient inside the sample's volume is distinguished from the topographic measurement of a 3D surface, for which various other methods are available such as light field imaging and time of flight imaging[8]. The 3D imaging methods are typically combined with a tunable filter (e.g., acousto-optic tunable filter, liquid-crystal tunable filter) to provide the 4D (3D structure and 1D spectrum) data cube. When a high spectral resolution is required, Fourier transform spectroscopy (FTS) is preferred, which obtains the spectrum of interrogated light from a series of interferograms recorded for varying optical path differences (OPDs)[9]. Hyperspectral 3D absorption imaging has been demonstrated by combining FTS with sample-rotation tomography in the infrared[10] and X-ray wavelength ranges[11]. In the visible wavelength range, a wavelength-scanning laser has been combined with beam-rotation tomography[12]. Additionally, studies have demonstrated spectroscopic optical coherence tomography to exhibit depth-resolved attenuation coefficient, the sum of absorption coefficient and scattering coefficient, for various wavelengths[13, 14].

Although hyperspectral 3D absorption imaging can provide the abundant structural and chemical information of a specimen, its adoption as a common inspection tool has been hampered due to the extremely low imaging throughput. The low imaging throughput is due to the need for scanning mechanisms for both changing the wavelength and obtaining the 3D image using sample rotation or beam rotation. The total data acquisition time to record the 4D data cube can take several hours for sample-rotation tomography and several tens of minutes for beam-rotation tomography. Importantly, various methods have been demonstrated to expedite the 3D imaging by collecting a multitude of the pro-

^{*} ysung4@uwm.edu

jection images in a single snapshot at the cost of spatial resolution[15–20]. In the pioneering work[15], Levoy et al. used a micro-lens array (MLA) to simulatenously capture the 4D light field (2D intensity and 2D propagation direction of light rays), from which the projection images for varying viewing angles can be synthesized. This technique called light-field microscopy (LFM) opened a new door to high-throughput volumetric imaging. Recently, the second class of LFM has been proposed. which includes Fourier integral microscopy (FIMic)[16], eXtended field of view LFM (XLFM)[17], and Fourier LFM (FLFM)[19]. These techniques commonly place the MLA at the Fourier plane (i.e., a plane conjugate to the back focal plane of the objective lens) and slightly differ in the location of the aperture stop and the reconstruction method. Snapshot projection optical tomography (SPOT)[20] may be considered as the third class of LFM, which arranges the MLA with the objective lens in a 4-f telecentric configuration and places an iris diaphragm at the back focal plane of a relay lens. This arrangement enables the single iris diaphragm to serve as the aperture stop for all the lenslets, and thereby achieves the dual telecentricity without sacrificing the light collection efficiency. It also allows for blocking stray rays from outside the field of view, which can otherwise contaminate the projection images. Snapshot holographic optical tomography (SHOT)[21] is distinguished from the others by placing the MLA in the illumination path for angular multiplexing[22]. These snapshot 3D tomography techniques offer new opportunities for high-throughput multidimensional imaging of microscopic specimens [23, 24]. We recently demonstrated 3D absorption imaging using SPOT and a carefully-designed illumination module [25]. Adding FTS, here we demonstrate hyperspectral 3D absorption imaging with moderate spatial resolution (1.3) μm), high spectral resolution (5 nm), and fast data acquisition speed (40 seconds for the entire 4D data cube).

II. SNAPSHOT OPTICAL TOMOGRAPHY FOR HYPERSPECTRAL 3D ABSORPTION IMAGING

A. System design

The instrument developed in this study consists of three parts: an illumination module, a SPOT system, and an FTS module. The illumination module was designed to generate focused light at the sample plane with a large convergence angle so that the sample is illuminated from all different directions. The SPOT system captures the light rays propagating along different directions to create a 2D array of projection images. The FTS module is used to obtain the spectrum at every point of the projection images. Figure 1(a) shows a schematic diagram of the illumination module. For the light source (LS), we used a high-power light emitting diode (Thorlabs, SOLIS-3C). The broadband light from the LS is fed to the illumination module using a liquid light guide (3

mm core diameter), which is focused onto the pinhole (P) with diameter of 600 µm using two achromats L1 and L2. The light after the pinhole is refocused onto the sample plane (SP) using the achromat L3 (f = 100 mm) and the oil-immersion condenser lens CL (Nikon, 1.4 NA). Figure 1(b) shows a schematic diagram of the SPOT system and the FTS module. A high-NA, oil-immersion objective lens (Nikon, Plan Apo VC 60X, 1.4 NA), OL, was used to record high-angle projection images. A micro-lens array (RPC Photonics, S600-f28), MLA, with the pitch of 600 µm and the focal length of 16.8 mm was placed in a 4f telecentric configuration with the OL. Between the OL and MLA, two relay lenses (not shown) with the demagnification of 2.5 times were inserted. For this design, 6 x 6 projection images were formed at the intermediate image plane, IIP1, i.e., the back focal plane of the MLA. Two achromatic lenses (L4 and L5) relayed the images from IIP1 to IIP2 and IIP3 through the beam splitter (BS) and with the magnification of 3.125. An iris diaphragm was inserted between L4 and L5, which served as the apertures stop for all the projection images. Another pair of achromats (L6 and L7) of the same focal length relayed the images from IIP2 and IIP3 to the image plane (IP), where the camera was located. For the FTS module, we tested both a plate beam splitter and a cube beam splitter. The chromatic aberration was less with the plate beam splitter; however, the interference fringes due to the plate surfaces made it difficult to choose. The lenses in the illumination module, the SPOT system, and the FTS module are achromats. All the lens pairs were arranged in 4-f telecentric configurations. Noteworthy, the FTS module was inserted between L4 and L7, so that a collimated beam incident onto the SP remains collimated as it propagates through the beam splitter; thereby, the chromatic aberration can be minimized. The mirror M1 was mounted on a translation stage (Physik Instrumente, P-721.CDQ) with the travel range of 100 µm, the resolution of 0.7 nm, and the repeatability of ± 5 nm. The stage was controlled in a closed loop using a capacitive sensor and a digital piezo controller (Physik Instrumente, E-709.CR). To record the images, we used a scientific complementary metal-oxide-semiconductor (sCMOS) camera (pco.edge 5.5) with the pixel size of 6.5 µm. For this design, the overall magnification was 39, the field of view 48 µm, and the pixel resolution 0.16 um. The lenslet NA was 0.22, and the diffraction limit was 1.3 µm for the wavelength of 600 nm.

B. Sample preparation

For the demonstration of imaging performance, we imaged 6 µm blue- and red-dyed polystyrene beads (Polysciences, 15715-5, 15714-5). A drop of undiluted bead solution was spread on a microscope slide (1 mm thickness) and covered with a No. 1 glass coverslip. The coverslip was fixed to the microscope slide with tape. For imaging single red blood cells (RBCs), a drop of blood

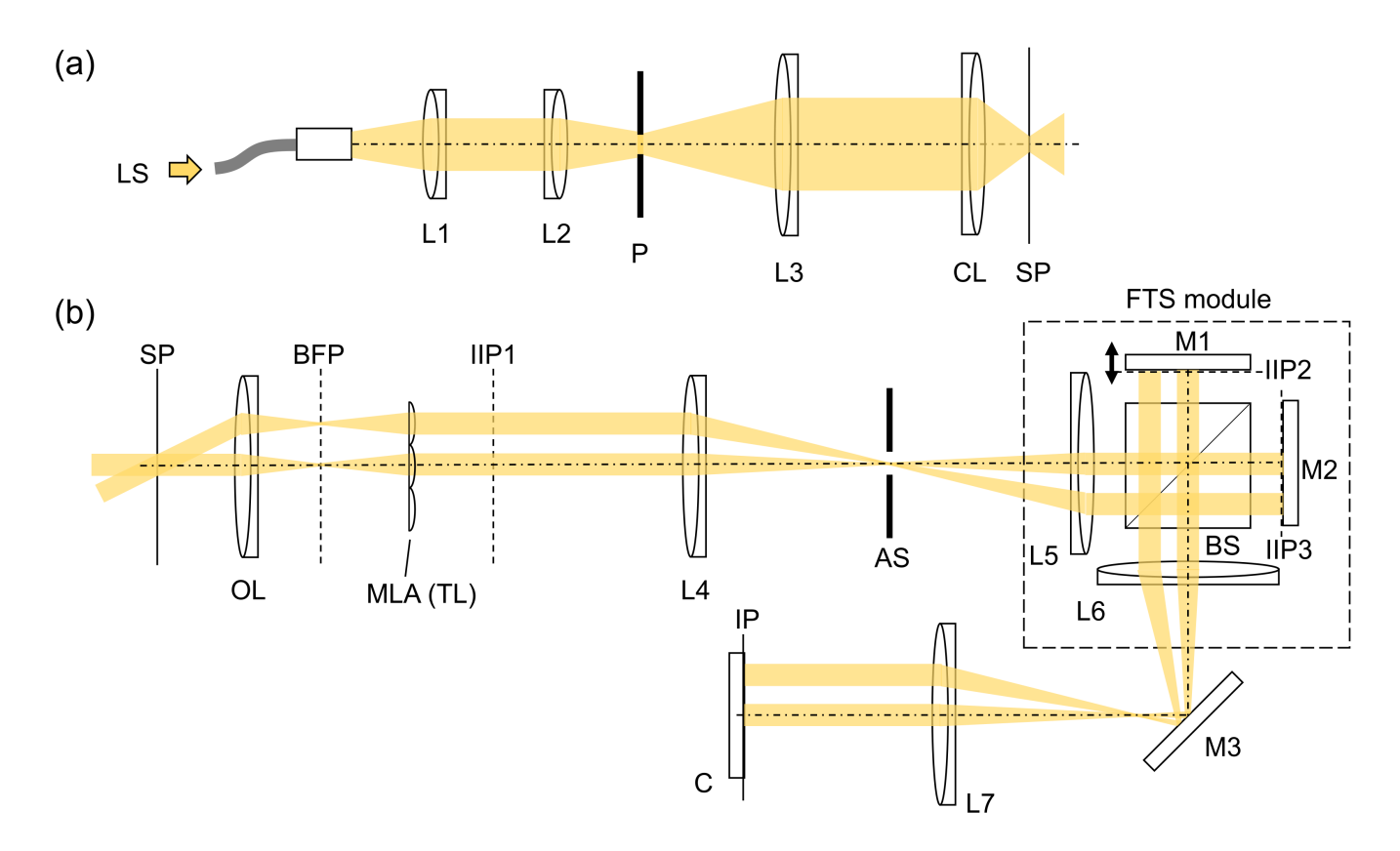


FIG. 1. Schematic diagram of the system developed in this study. (a) Illumination module, and (b) hyperspectral SPOT system. LS: light source; L1-L7: lenses; M1-M3: mirrors, OL: objective lens; MLA: micro-lens array; TL: tube lens; BS: beam splitter; AS: aperture stop; SP: sample plane; BFP: back-focal plane of OL; IIP1-IIP3: intermediate image planes; and IP: image plane. Two emission beam paths are traced from a point-like emitter at the sample plane to the image plane.

was obtained from a healthy adult donor and mixed in a 1.5-mL tube with 1 mL of $1\times$ phosphate-buffered saline (PBS; Corning, 21-040-CV) without calcium and magnesium. For oxygenated RBCs, 20 μL of blood solution was pipetted out from the tube, spread on a microscope slide, and covered with a No. 1 glass coverslip. For deoxygenated RBCs, 200 μL of blood solution was mixed in a 1.5-mL tube with the same volume of 2 % sodium metabisulfite (Sigma, 799343-500G) solution (dissolved in distilled water). Then, 20 μL of the mixed solution was pipetted out from the tube, spread on a microscope slide, and covered with a No. 1 glass coverslip. The experimental protocol using human blood was approved by the Institutional Review Board at the University of Wisconsin-Milwaukee.

C. Data acquisition

For the observation, we mounted the sample on the translation stage of the microscope, then adjusted the objective focus using one of the projection images near the center. The axial position of the condenser lens was adjusted to have the sample located in the center in all the projection images. The exact location of the con-

denser lens is not critical, as the projection images are co-registered in the data processing step. For FTS, two copies of the projection images formed at IIP2 and IIP3 need to overlap on the camera, for which the orientations of the mirrors M1 and M2 were adjusted. After the initial alignment, the scanning mirror M1 was axially moved to the center of travel range. Then, the axial position of the mirror M2 was manually moved to the zero-OPD position while monitoring the image intensity on the camera; the intensity is the highest when M2 is at the zero-OPD position. For each sample, 1000 interferogram images were acquired with the step size of 50 nm; the total travel range was 50 µm, which corresponds to the OPD of 100 μm . The images were recorded in a global shutter mode with the camera exposure time of 0.5 msec and the dynamic range of 16 bit. The total data acquisition time was about 40 seconds. We used LabVIEW (National Instruments, version 15) for synchronous control of the translation stage and the camera. The stack of images shown in Figure 2(a) represents the raw interferogram images recorded for varying OPDs. One of the interferogram images consisting of 32 projection images is shown as an example, which was acquired for a 6 µm blue-dyed bead. One of the projection images is magnified and shown on the right. Figure 2(b) shows the

detector counts for varying OPDs at two locations in the magnified image: (i) one within the bead region and (ii) the other in the background region.

D. Data processing

The raw interferogram images were first processed with the FTS data processing as follows. The translation stage positions recorded during data acquisition are loaded along with the interferogram images of the projection images, which are saved into arrays as interferograms at each pixel. The interferograms are shifted along the stage coordinate axis so that the peak of the envelope of the interferogram is at the center. The interferograms are detrended and apodized with the Norton-Beer medium apodization function[9]. The Fourier transform is computed by the non-uniform fast Fourier transform (NUFFT) function[26], resulting in the spectral intensity of the sample projection images at selected wavelengths. Figure 3(a) shows a stack of spectral images, each of which consists of 32 projection images. One of the spectral images at 600 nm is shown in Figure 3(a) (i) and a magnified image is shown in (ii) as an example. These images were obtained by applying the FTS data processing to the data shown in Figure 2(a). One of the projection images is magnified and shown on the right. Figure 3(b) shows the fluorescence emission spectra measured at the same two locations in the magnified image: (i) one within the bead region and (ii) the other in the background region.

The grid of projection images is automatically detected using a threshold to find a binary mask, then using a built-in circle finding algorithm of MATLAB (Mathworks, Inc., version R2021a) to find the inner illumination regions. The oval outer illumination regions are found by extrapolating the average distances between the inner illumination regions. These images are coregistered automatically using a built-in MATLAB function for the intensity-based image registration. The projection images are then normalized with the background images by elementwise division at each pixel. These normalized projection images are detrended and deblurred using Richardson-Lucy deconvolution implemented as a built-in MATLAB function. The viewing angle of each projection image can be calculated from its location in the array and the focal length of the objective lens. The 2D Fourier-transform of each projection image is found using the 2D fast Fourier transform. The Fourier transforms of the projection images are mapped onto their corresponding planes resulting in a 3D array. After regularization using the positivity constraint[27], the 3D inverse Fourier transform is performed, which results in a 3D absorption map. More detailed explanation of the reconstruction process and related theory can be found in our recent paper [25]. This process is repeated, providing the 3D absorption profile for each wavelength.

III. RESULTS AND DISCUSSION

Using the developed system, we imaged blue- and reddyed polystyrene beads of 6 µm diameter. Figure 4 shows an example of tomographic reconstruction: a horizontal (a) and a vertical (b) cross section of the 3D absorption map for the bead at 600 nm, and 2D cross sectional slices at 0.85 µm intervals (c) from the 3D reconstructed image. The horizontal cross section shows a uniform distribution of absorption coefficient within most of the bead region. The value slightly decreases at the boundary due to the moderate spatial resolution (1.3 µm). The bead is shown shrunk along the optical axis direction (Z) due to the regularization, which was used to mitigate the missing-cone artefact originating from the limited angular coverage. The missing-cone artefact of beam-rotation tomography and the regularization to suppress it has been extensively studied[28]. Figure 5(a) shows the measured absorption spectra of the blue- and red-dyed beads in the wavelength range of 450 – 700 nm at 10 nm wavelength steps. The sample size was 5 for each bead type. In Figures 5(a) and 5(b), the centerline is the mean, and the shaded band represents the standard deviation. The shapes of the curves match well with our previous measurements on similar dyed beads (Phosphorex, 1010KB and 1010KR), which were acquired using beam-rotation tomography in tandem with a wavelength-scanning laser source[12].

To demonstrate the potential for imaging biological samples, we imaged single RBCs with the developed system. Figure 5(b) shows the absorption spectra of oxygenated and deoxygenated RBCs for the same wavelength range of 450 - 700 nm. The wavelength step size was reduced to 5 nm to capture the characteristic peaks of the absorption spectra. For the oxygenated RBCs, the shape of a flattened biconcave disc was easily lost in the imaging chamber, and we frequently observed echinocytes with a very different shape from the discocytes. Thus, we were able to collect a smaller number of oxygenated RBCs (the sample size, n=3) than deoxygenated RBCs (n = 6). Nevertheless, the average absorption spectrum for oxygenated RBCs clearly shows the hemoglobin Q bands at 540 and 575 nm, and its standard deviation is as small as that for deoxygenated RBCs. The absorption coefficients at the observed peaks are 22.06 \pm 8.88 mm^{-1} at 540 nm and 25.07 \pm 5.45 mm^{-1} at 575 nm. For deoxygenated RBCs, the two bands are fused to form one peak at 555 nm, at which the absorption coefficient is $22.80 \pm 7.39 \ mm^{-1}$. In our previous study[12], the absorbance peaks representing the hemoglobin Q bands for the oxygenated RBCs were also observed at 540 nm and 575 nm and the single fused peak of 555 nm for the deoxygenated RBC. The measured absorption coefficients are lower than the values that we previously obtained using beam-rotation tomography. The difference may be attributed to the small number of projection images (32 instead of 200), a biological variation, or both. Importantly, the method we demonstrate in this paper has much higher throughput

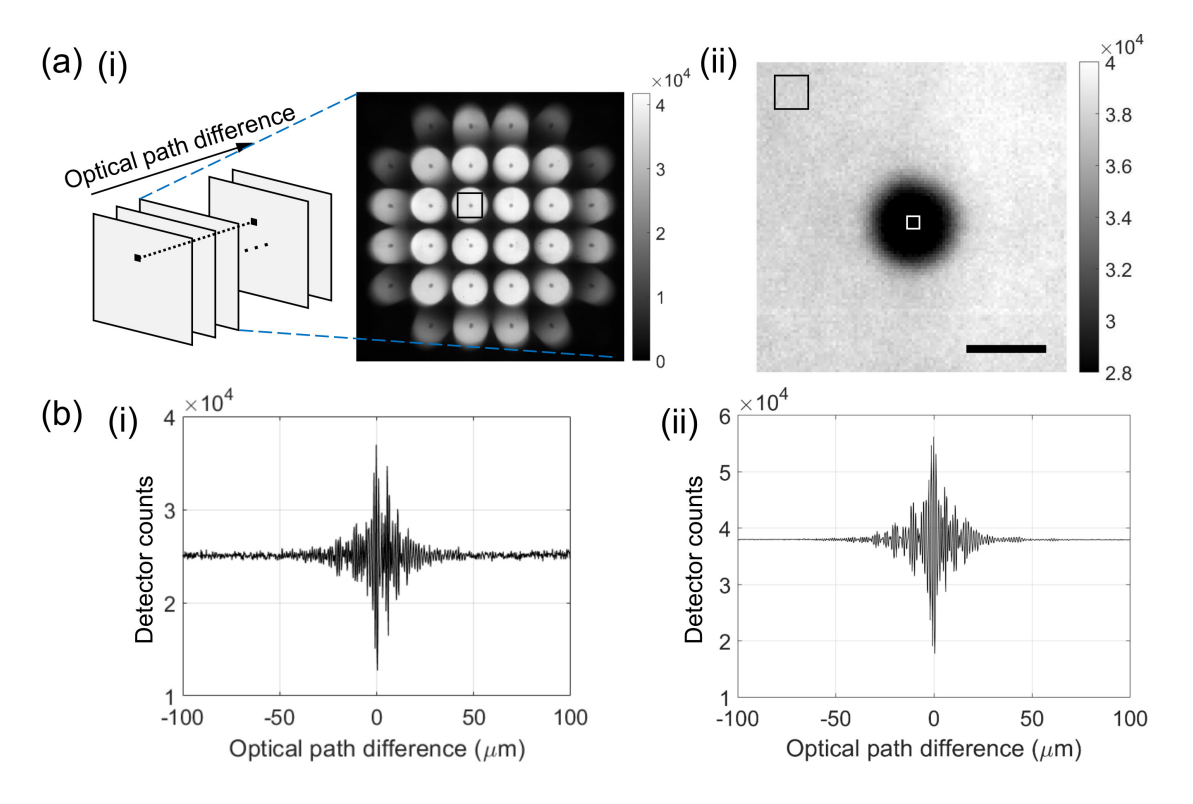


FIG. 2. Example raw images acquired with the developed system. (a) An example interferogram image (i) acquired for a 6 μm blue-dyed bead, which consists of a multitude of projection images. One of the projection images (marked as a square) is magnified and shown on the right (ii). Scale bar: 5 μm. (b) Example interferograms at the center of bead (i) and the background region (ii).

(40 seconds instead of about 20 minutes) while providing the same information. This massive improvement in throughput is enabled by collecting the projection images in a single snapshot. The speed is limited by the FTS system, specifically capturing 1000 interferogram images to achieve high spectral resolution. Noteworthy, we have shown that deep learning can greatly reduce the interferogram sampling in FTS[29]. This leaves the potential for further increasing the throughput of the developed system, which is left for our future work.

We previously demonstrated hyperspectral 3D fluorescence imaging using SPOT and FTS[24]. Here we have demonstrated hyperspectral 3D absorption imaging, which is enabled by two major improvements. First, we have combined SPOT with a carefully-designed illumination module to allow for 3D absorption imaging in a single snapshot. The method demonstrated with a quasimonochromatic LED is extended here to hyperspectral 3D absorption imaging[25]. Second, we have achromatized the entire system by replacing all the plano-convex lenses except for MLA with achromats and moving the FTS module from a Fourier plane to an intermediate image plane. Before these changes, the projection images after the FTS processing were completely misaligned across the wavelengths. Figure 6(a) shows an example, which is a montage of the projection images reconstructed for 26 wavelengths from 450 nm to 700 nm (10

nm step size). After the achromatization, we were able to record the projection images with better, though not perfect, alignment across the wavelengths, as shown in Figure 6(b). The remaining misalignment may be attributed to the chromatic aberration of the MLA, the only component that we could not replace with an achromat. Using the developed system, we imaged blue- and red-dyed microspheres of 6 µm diameter. Although the spatial resolution was moderate, we were able to reconstruct the beads' horizontal and vertical cross sections with the accuracy similar to that of beam-rotation tomography[12]. Further, we measured the absorption coefficients of oxygenated and deoxygenated RBCs from the reconstructed 4D maps, demonstrating the potential for this system to be used for other biological specimens without dyes.

Hyperspectral imaging allows visualization of multiple biological markers within a single tissue specimen[30–32]. It has also been shown to provide higher sensitivity and specificity than conventional three-color (RGB) imaging in the histopathological analysis of samples and disease detection[33, 34]. Hyperspectral imaging in the infrared range has been used for various applications such as classification and quantification of the type and amount of lipids in a biofuel-producing algae cell[35], or classifying and quantifying microplastics found in drinking water, which is a topic of growing concern[36–38]. Hyperspectral 3D absorption imaging demonstrated here allows ac-

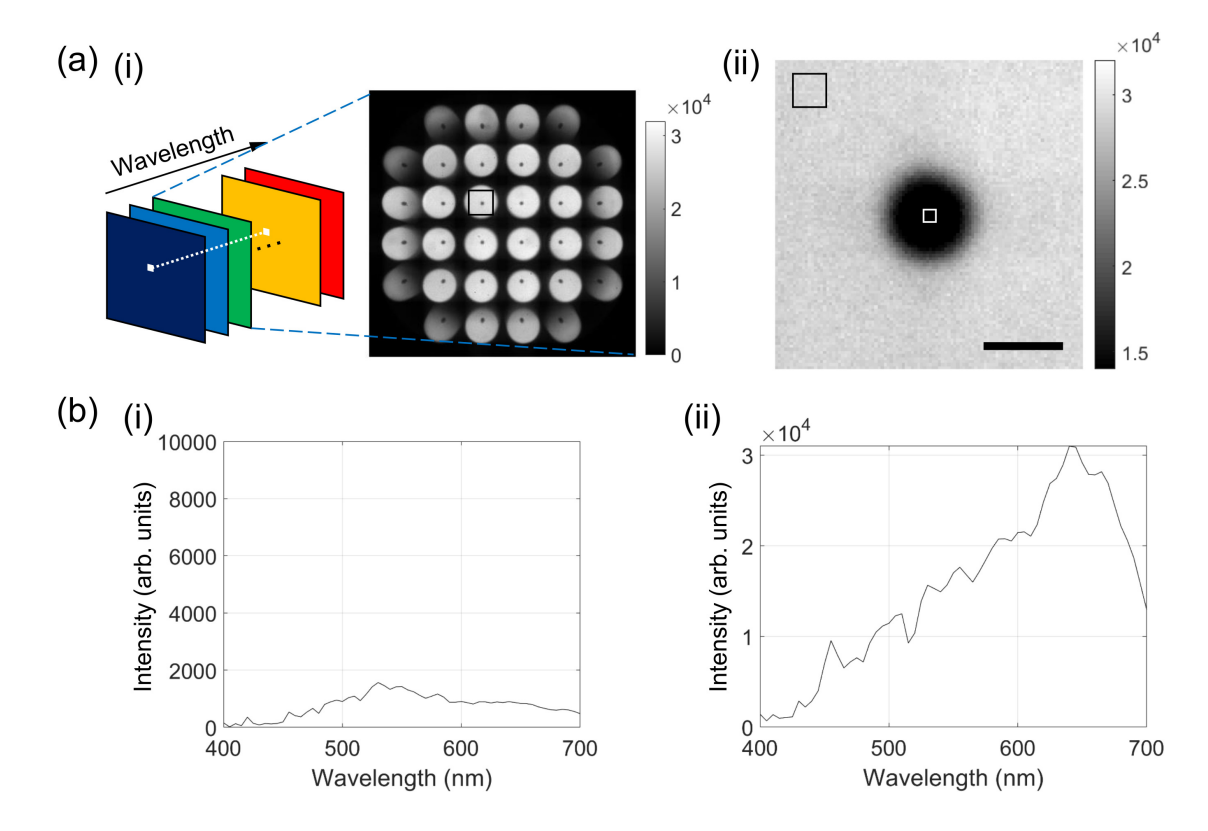


FIG. 3. Fourier-transform spectroscopy (FTS) data processing. (a) An example absorption image (i) at the wavelength of 600 nm, which was reconstructed from the raw interferogram images in Fig. 2(a). One of the projection images (marked as a square) is magnified and shown on the right (ii). Scale bar: 5 μm. (b) Example spectra at the center of bead (i) and the background region (ii).

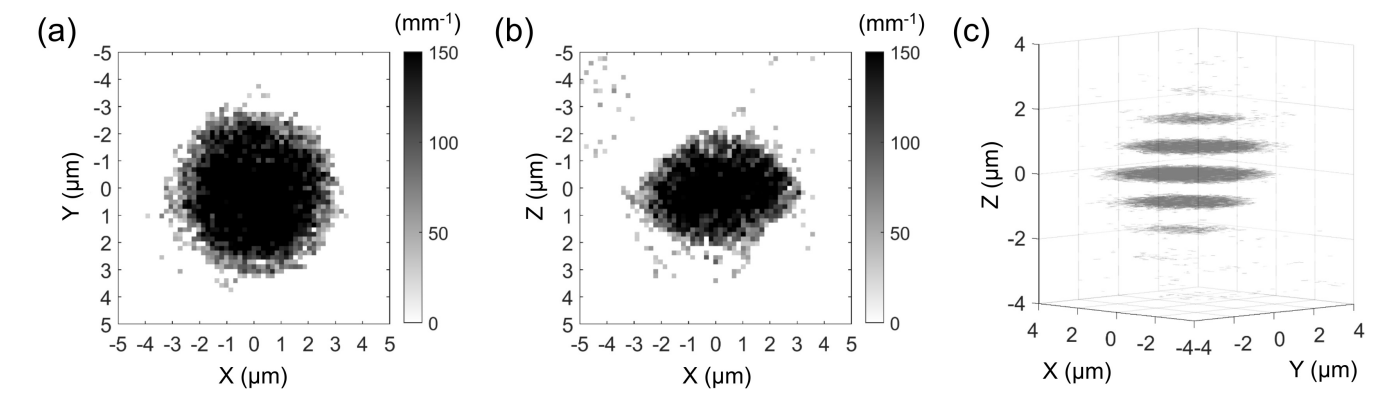


FIG. 4. Snapshot projection optical tomography (SPOT) data processing. A horizontal (a) and a vertical (b) cross section of a 6 μ m blue-dyed bead reconstructed at the wavelength of 600 nm. (c) Horizontal cross-sectional slices along the Z axis. (X,Y,Z) are the Cartesian coordinates with Z being the optical axis direction.

cess to each voxel in the 3D volume. This additional dimension of information allows for more accurate classification and quantification of complex, nonhomogeneous specimens at micrometer scales. With the high throughput of the demonstrated system, acquiring the 4D data cube is now feasible for many applications, in which the sample rapidly change the morphology or chemical composition, and thus must be imaged in a certain time win-

dow.

IV. CONCLUSION

We have developed an optical system which has the capability of measuring the 3D structural and chemical information of a sample with high throughput and

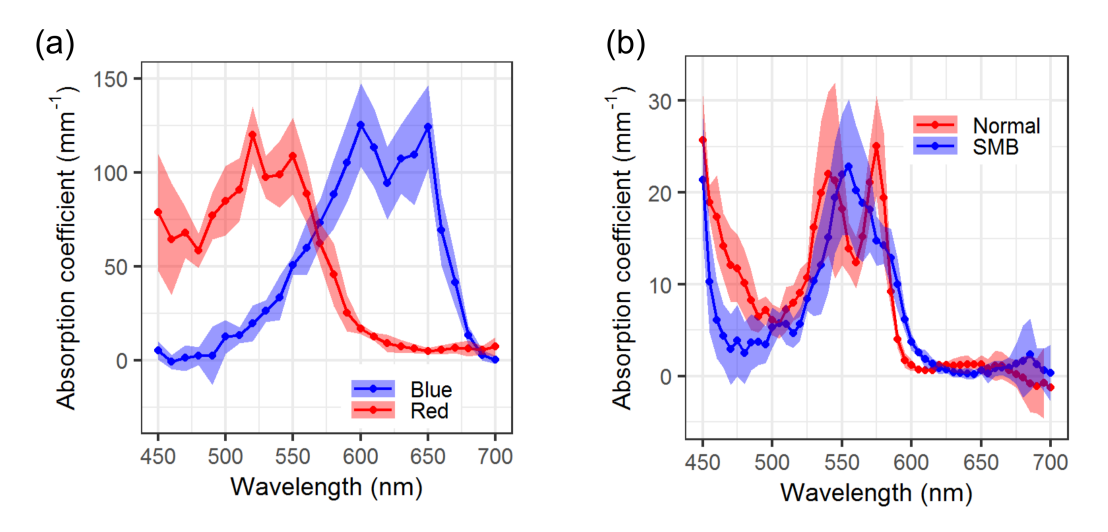


FIG. 5. Absorption coefficient of dyed beads and red blood cells (RBCs). (a) Absorption spectra of the blue- and red-dyed beads, and (b) absorption spectra of the oxygenated- and deoxygenated-RBCs (labeled as SMB).

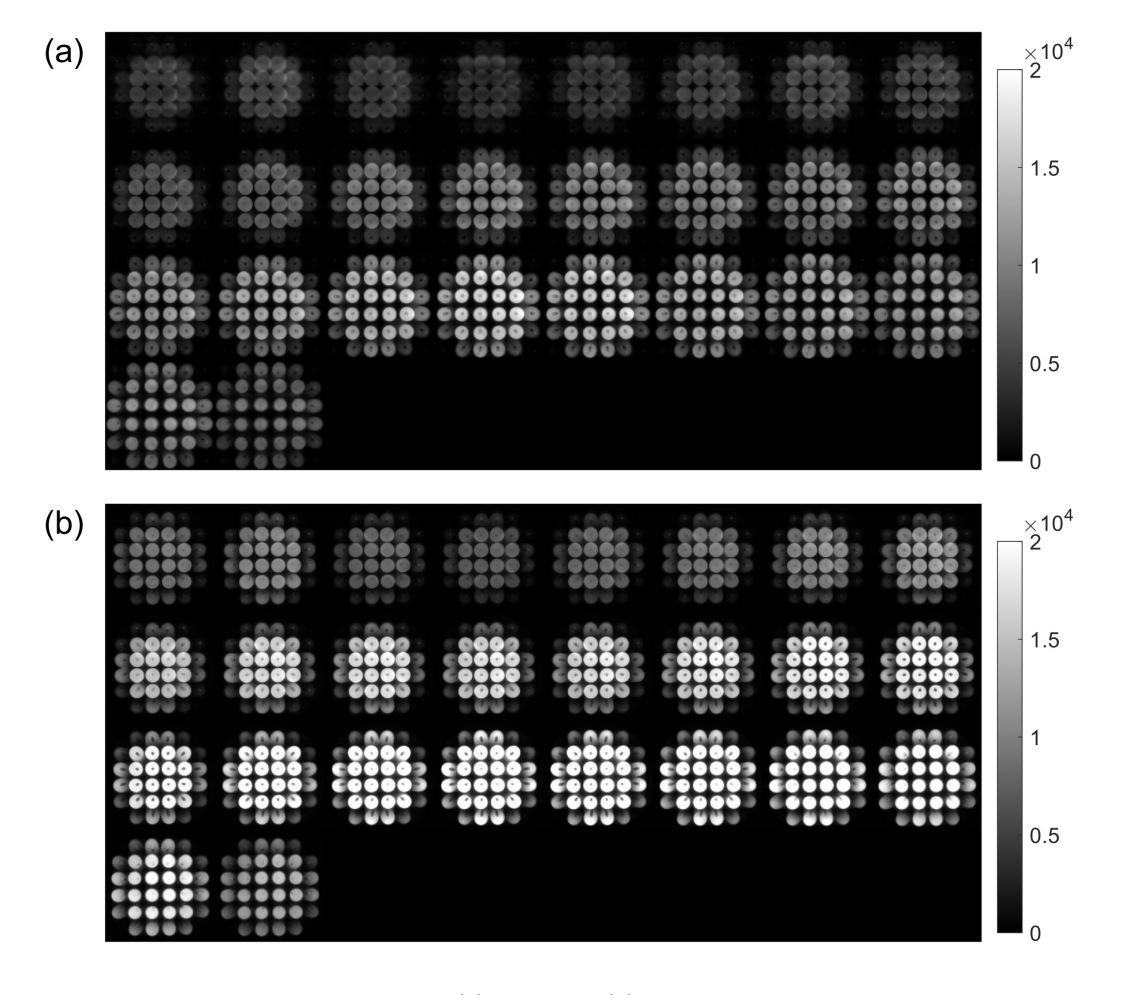


FIG. 6. Example hyperspectral image stacks before (a) and after (b) the achromatization. The sample is a 6 μ m blue-dyed bead, and each figure shows a montage of the projection images reconstructed for 26 wavelengths from 450 nm to 700 nm (10 nm step size). The colorbar indicates the intensity in arbitrary units.

specificity. The hyperspectral 3D imaging system was demonstrated by imaging dyed microspheres and oxygenated and deoxygenated red blood cells. The measured absorption coefficient spectra matched previously published data obtained with a wavelength-scanning laser and beam rotation tomography. With the combination of SPOT for single-shot 3D imaging and FTS for high spectral resolution, the developed system has a potential to be used for many applications including absorbance-based chemical analysis and label-free, high-content imaging of

biological specimens.

ACKNOWLEDGMENTS

This research was funded by the Research Growth Initiative of the University of Wisconsin-Milwaukee, the National Science Foundation (1808331), and the National Institute of General Medical Sciences of the National Institutes of Health (R21GM135848). Any opinions, findings, and conclusions or recommendations expressed in this material are those of the author and do not necessarily reflect the views of the National Institutes of Health.

- S. M. Nilapwar, M. Nardelli, H. V. Westerhoff, and M. Verma, Absorption spectroscopy, Methods Enzymol. 500, 59 (2011).
- [2] P. Zachee, J. Snauwaert, P. Vandenberghe, L. Hellemans, and M. Boogaerts, Imaging red blood cells with the atomic force microscope, Br. J. Haematol. 95, 472 (1996), publisher: Wiley Online Library.
- [3] N. A. Hagen and M. W. Kudenov, Review of snapshot spectral imaging technologies, Opt. Eng. 52, 090901 (2013).
- [4] G. Lu and B. Fei, Medical hyperspectral imaging: a review, J. Biomed. Opt. 19, 010901 (2014).
- [5] W. R. Johnson, D. W. Wilson, W. Fink, M. S. Humayun, and G. H. Bearman, Snapshot hyperspectral imaging in ophthalmology, J. Biomed. Opt. 12, 014036 (2007).
- [6] M. E. Gehm, R. John, D. J. Brady, R. M. Willett, and T. J. Schulz, Single-shot compressive spectral imaging with a dual-disperser architecture, Opt. Express 15, 14013 (2007).
- [7] A. C. Kak and M. Slaney, Principles of computerized tomographic imaging (SIAM, 2001).
- [8] Y. Hu, Q. Chen, S. Feng, and C. Zuo, Microscopic fringe projection profilometry: A review, Opt. Lasers Eng. 135, 106192 (2020).
- [9] P. R. Griffiths and J. A. De Haseth, Fourier transform infrared spectrometry, Vol. 171 (John Wiley & Sons, Hoboken, NJ, 2007).
- [10] M. C. Martin, C. Dabat-Blondeau, M. Unger, J. Sedlmair, D. Y. Parkinson, H. A. Bechtel, B. Illman, J. M. Castro, M. Keiluweit, and D. Buschke, 3D spectral imaging with synchrotron Fourier transform infrared spectromicrotomography, Nat. Methods 10, 861 (2013).
- [11] M. Obst, J. Wang, and A. P. Hitchcock, Soft X-ray spectro-tomography study of cyanobacterial biomineral nucleation, Geobiology 7, 577 (2009).
- [12] Y. Sung, Spectroscopic microtomography in the visible wavelength range, Phys. Rev. Appl. 10, 054041 (2018).
- [13] U. Morgner, W. Drexler, F. X. Kärtner, X. D. Li, C. Pitris, E. P. Ippen, and J. G. Fujimoto, Spectroscopic optical coherence tomography, Opt. Lett. 25, 111 (2000).
- [14] A. L. Oldenburg, C. Xu, and S. A. Boppart, Spectroscopic optical coherence tomography and microscopy, IEEE J. Sel. Topics Quantum Electron. 13, 1629 (2007).
- [15] M. Levoy, R. Ng, A. Adams, M. Footer, and M. Horowitz, Light field microscopy, ACM Trans. Graph., 924 (2006).

- [16] A. Llavador, J. Sola-Pikabea, G. Saavedra, B. Javidi, and M. Martínez-Corral, Resolution improvements in integral microscopy with Fourier plane recording, Opt. Express 24, 20792 (2016).
- [17] L. Cong, Z. Wang, Y. Chai, W. Hang, C. Shang, W. Yang, L. Bai, J. Du, K. Wang, and Q. Wen, Rapid whole brain imaging of neural activity in freely behaving larval zebrafish, Elife 6, e28158 (2017).
- [18] G. Scrofani, J. Sola-Pikabea, A. Llavador, E. Sanchez-Ortiga, J. C. Barreiro, G. Saavedra, J. Garcia-Sucerquia, and M. Martínez-Corral, FIMic: design for ultimate 3D-integral microscopy of in-vivo biological samples, Biomed. Opt. Express 9, 335 (2018).
- [19] C. Guo, W. Liu, X. Hua, H. Li, and S. Jia, Fourier light-field microscopy, Optics express 27, 25573 (2019), publisher: Optical Society of America.
- [20] Y. Sung, Snapshot projection optical tomography, Phys. Rev. Appl. 13, 054048 (2020).
- [21] Y. Sung, Snapshot holographic optical tomography, Physical Review Applied 11, 014039 (2019).
- [22] A. Kuś, Real-time, multiplexed holographic tomography, Optics and Lasers in Engineering 149, 106783 (2022), publisher: Elsevier.
- [23] J. Wu, B. Xiong, X. Lin, J. He, J. Suo, and Q. Dai, Snapshot hyperspectral volumetric microscopy, Scientific reports 6, 1 (2016), publisher: Nature Publishing Group.
- [24] C. Juntunen, I. M. Woller, and Y. Sung, Hyperspectral Three-Dimensional Fluorescence Imaging Using Snapshot Optical Tomography, Sensors 21, 3652 (2021), publisher: Multidisciplinary Digital Publishing Institute.
- [25] Y. Sung, Snapshot three-dimensional absorption imaging of microscopic specimens, Phys. Rev. Appl. 15, 064065 (2021).
- [26] A. Dutt and V. Rokhlin, Fast Fourier transforms for nonequispaced data, SIAM J. Sci. Comput. 14, 1368 (1993).
- [27] Y. Sung and R. R. Dasari, Deterministic regularization of three-dimensional optical diffraction tomography, J. Opt. Soc. Am. A 28, 1554 (2011), publisher: Optical Society of America.
- [28] A. M. Taddese, N. Verrier, M. Debailleul, J.-B. Courbot, and O. Haeberlé, Optimizing sample illumination scanning in transmission tomographic diffractive microscopy, Appl. Opt. 60, 1694 (2021).

- [29] C. Juntunen, I. M. Woller, A. R. Abramczyk, and Y. Sung, Deep-learning-assisted Fourier transform imaging spectroscopy for hyperspectral fluorescence imaging, Sci. Rep. 12, 2477 (2022).
- [30] M. J. Campbell, F. Baehner, T. O'Meara, E. Ojukwu, B. Han, R. Mukhtar, V. Tandon, M. Endicott, Z. Zhu, and J. Wong, Characterizing the immune microenvironment in high-risk ductal carcinoma in situ of the breast, Breast Cancer Res. Treat. 161, 17 (2017).
- [31] Z. Feng, D. Bethmann, M. Kappler, C. Ballesteros-Merino, A. Eckert, R. B. Bell, A. Cheng, T. Bui, R. Leidner, and W. J. Urba, Multiparametric immune profiling in HPV-oral squamous cell cancer, JCI insight 2 (2017).
- [32] C. Jiang, Y.-H. Huang, J.-B. Lu, Y.-Z. Yang, H.-L. Rao, B. Zhang, W.-Z. He, and L.-P. Xia, Perivascular cell coverage of intratumoral vasculature is a predictor for bevacizumab efficacy in metastatic colorectal cancer, Cancer Manag. Res. 10, 3589 (2018).
- [33] S. Ortega, M. Halicek, H. Fabelo, G. M. Callico, and B. Fei, Hyperspectral and multispectral imaging in digital and computational pathology: a systematic review, Biomed. Opt. Express 11, 3195 (2020), publisher: Optical Society of America.
- [34] S. Ortega, M. Halicek, H. Fabelo, R. Camacho, M. d. l. L. Plaza, F. Godtliebsen, G. M Callicó, and B. Fei,

- Hyperspectral imaging for the detection of glioblastoma tumor cells in H&E slides using convolutional neural networks, Sensors **20**, 1911 (2020), publisher: Multidisciplinary Digital Publishing Institute.
- [35] L. M. Laurens and E. J. Wolfrum, Feasibility of spectroscopic characterization of algal lipids: chemometric correlation of NIR and FTIR spectra with exogenous lipids in algal biomass, Bioenergy Res. 4, 22 (2011), publisher: Springer.
- [36] A. A. Koelmans, N. H. M. Nor, E. Hermsen, M. Kooi, S. M. Mintenig, and J. De France, Microplastics in freshwaters and drinking water: Critical review and assessment of data quality, Water Res. 155, 410 (2019), publisher: Elsevier.
- [37] E. Danopoulos, M. Twiddy, and J. M. Rotchell, Microplastic contamination of drinking water: A systematic review, PLoS One 15, e0236838 (2020), publisher: Public Library of Science San Francisco, CA USA.
- [38] M. Pivokonsky, L. Cermakova, K. Novotna, P. Peer, T. Cajthaml, and V. Janda, Occurrence of microplastics in raw and treated drinking water, Sci. Total Environ. 643, 1644 (2018), publisher: Elsevier.